



Influence of Mn content on the morphology and improved electrochemical properties of $\text{Mn}_3\text{O}_4|\text{MnO}@\text{carbon}$ nanofiber as anode material for lithium batteries

Gang Yang ^{a,b,*}, Yuhong Li ^a, Hongmei Ji ^a, Haiying Wang ^a, Po Gao ^{a,c}, Lu Wang ^c, Haidong Liu ^a, João Pinto ^b, Xuefan Jiang ^a

^a Jiangsu Laboratory of Advanced Functional Material, Changshu Institute of Technology, Changshu 215500, PR China

^b Department of Physics, I3N, University of Aveiro, 3810-193 Aveiro, Portugal

^c School of Material Science and Engineering, Jiangsu University of Science and Technology, Zhenjiang 212003, PR China

HIGHLIGHTS

- Composites $\text{MnO}_x/\text{carbon}$ synthesized through thermal stabilization and carbonization.
- Phase composition, morphology and capacity affected by Mn concentration in precursor.
- Mn33_3h with the lowest manganese content presents the best electrochemical properties.
- Discharge capacity of Mn33_3h at the 50th cycle remains 99.7% of that at the 2nd cycle.
- Composite structure of $\text{MnO}_x/\text{carbon}$ is efficient to improve capacity and cycleability.

ARTICLE INFO

Article history:

Received 28 February 2012

Received in revised form

24 May 2012

Accepted 28 May 2012

Available online 1 June 2012

Keywords:

Manganese oxides

Carbon fiber

Composite structure

Anode materials

Lithium batteries

ABSTRACT

A series of composites manganese oxide/carbon with one-dimensional structure are synthesized using electrospinning. The phase composition, morphology and electrochemical performance of $\text{MnO}_x/\text{carbon}$ are studied, which affected by the manganese concentration in precursor and subsequent carbonization conditions. The manufacture of $\text{MnO}_x/\text{carbon}$ is composed of two steps including thermal stabilization (at 250 °C in air) and carbonization (at 700 °C in nitrogen). The main functional groups of samples are well identified by FT-IR spectra. The sample Mn33_3h with the lowest manganese content presents the construction structure which amorphous and/or nanosized MnO_x with smaller crystal size are grown and enwrapped in carbon fiber during carbonization. Mn33_3h presents the initial charge and discharge capacities of 1054.1 and 665.6 mAh g⁻¹, and the discharge capacity at the 50th cycle remains 99.7% of that at the 2nd cycle. Beside the well rate capability at the range of current densities from 20 to 1000 mA g⁻¹, Mn33_3h presents very good recovery ability after high rate cycling at 1000 mA g⁻¹. The advantages of this composite structure as well as its high capacity make manganese oxide a very attractive candidate as an anode material for the next generation of rechargeable lithium ion batteries.

© 2012 Elsevier B.V. All rights reserved.

1. Introduction

Secondary lithium batteries, the most rapidly growing power sources, have been widely used in portable electronic devices. They are also a very promising energy storage device to meet the fast

emerging demands in plug-in electric vehicles and integrated grid systems [1]. To further improve the ability of the current lithium ion battery, it is essential to use high-capacity cathode and anode materials. Commercial anodes for lithium batteries mostly comprise of graphite since it offers both electrochemical and mechanical stability, but which provides a capacity of 372 mAh g⁻¹ upon lithiation [2]. New anode materials with higher capacity, such as silicon, tin and transition metal oxides, have attracted more interest to replace the current carbon-based anodes [3]. Transition metal oxides as anode materials were first proposed by Poizot et al. [4]. And then, nanomaterials of metal oxides, such as Co_3O_4 , SnO_2 ,

* Corresponding author. Jiangsu Laboratory of Advanced Functional Material, Changshu Institute of Technology, Changshu 215500, PR China. Tel.: +86 512 52251895; fax: +86 512 52251842.

E-mail addresses: gyang@cslg.edu.cn, yanggang9989@yahoo.com.cn (G. Yang).

FeO_x , and NiO [4–10], have been intensively studied as anode materials for lithium ion batteries aimed at achieving higher specific capacities than graphite. Transition metal oxides are used as anode due to the high electrochemical capacity, good capacity retention and high rate performance. Among all the metal oxides that can be used as anode for lithium batteries, manganese oxides have attracted great attention due to their high theoretical capacity, lower electromotive force, environmental benignity and natural abundance [11–16].

However, beside low electrical conductivity manganese oxides have the similar disadvantages that the anodes based on pure transition metal or metal oxides suffer from poor cycling performance [17,18]. The main reason is owing to their agglomerations and mechanical instabilities caused by the huge volume change and aggregation during lithium insertion and extraction processes, resulting in increased diffusion lengths and electrical disconnection from collector [19,20]. To overcome these challenges, extensive research has been devoted, such as reducing the particle size of manganese oxides to the nanometer scale, preparing composites, coating carbons, and adding electronically conductive materials, etc. [12–15,21–23]. Abruna's group synthesized spongelike nanosized Mn_3O_4 which shown a high initial reversible capacity (869 mAh g^{-1}) and the coulombic efficiency for the first cycle reaches more than 65% and remains at over 95% in the subsequent cycles [22]. Z. Lin et al. prepared composite MnO_x/CNFs by electrodepositing MnO_x nanoparticles on the surface of carbon nanofibers (CNFs) [23]. The reversible capacity of MnO_x/CNFs at the 2nd and 50th cycle is about 558 and 444 mAh g^{-1} , about 90% and 72% retention of the initial value (618 mAh g^{-1}). It indicated that nanosized MnO_x depositing on CNFs improves the capacity due to the increasing of conductivity, but huge volume change and aggregation during lithium insertion and extraction were still unresolved which resulted in the poor cycle performance. Zhong et al. reported a layer of the solid electrolyte interphase with a thickness of 20–60 nm was covered on MnO particles after full insertion. MnO powder materials show reversible capacity of 650 mAh g^{-1} [13].

In our previous work, $\text{Sn}|\text{SnO}_2$ nanoparticles enwrapped in carbon nanofibers were synthesized by using electrospinning and carbonization treatment, which presented great improved capacity and very well cycle performance [10]. The structure of metal and metal oxide nanoparticles dispersed and limited inside the carbon fibers has several advantages, first, the carbon fibers to provide higher specific surface area, well electrical contact and lithium ion conductivity; second, adequate void space (as a “buffer zone”) in carbon fibers to flexible accommodate the large volume change in the lithiation and delithiation [10,24]. The relatively separated tin nanoparticles inside the carbon fibers are retarded the aggregation during the Li alloying accompanied with volume change, and demonstrate a well cycle performance. Results are demonstrated that the morphology and diameter of electrospun polymer fibers are depended on the concentration and the additive material. Hsiao et al. reported proper concentration and charge density of the salt solution favored the formation of uniform smaller nanofibers without bead-like textures [25]. Metal component plays two roles in electrospinning, one is as the salt solution with various concentrations to control the morphology of composite fibers, and the other is to form metallic or metal oxide as the anode material after heat-treatment.

In this work, we synthesize a series of one-dimensional nanostructural materials of manganese oxide nanoparticles enwrapped in carbon nanofibers, considering the special structure of nanoparticles dispersed in carbon matrix is an efficient way to improve the cell capacity and cycleability. The composition of manganese phase, morphology and the formation mechanism of

$\text{MnO}|\text{Mn}_3\text{O}_4@\text{carbon}$ nanofibers are studied by X-ray diffraction patterns (XRD), scanning electron microscopy (SEM), and Fourier transform infrared spectroscopy (FT-IR) analysis. The electrochemical performance of the as-synthesized samples is discussed in detail.

2. Experimental procedures

The reagents of polyacrylonitrile (PAN, $M_w = 150,000$) and manganese acetate tetrahydrate ($\text{MnAc}_2 \cdot 4\text{H}_2\text{O}$, 99.0%) are used without further purification. Dimethylformamide (DMF) is used as solvent. In this work, firstly the film of MnAc_2/PAN nanofiber is synthesized using electrospinning, and the following carbonization is very important for composition and electrochemical performance of $\text{MnO}|\text{Mn}_3\text{O}_4@\text{carbon}$ nanofibers (simply noted as $\text{MnO}_x/\text{carbon}$).

The preparation of samples included three parts is listed in Table 1. (1) The precursors with four different starting weight ratio of MnAc_2 and PAN are carbonized at 700 °C for 3 h; (2) the precursors with the starting weight ratio of MnAc_2 and PAN (1:2) carbonized at 700 °C for 1, 3, 6 and 12 h, respectively; (3) the precursors with the starting weight ratio of MnAc_2 and PAN (1:2) carbonized for 3 h at 500, 600, 700, and 800 °C, respectively. The routes of the above preparation are described as following.

In a typical procedure, PAN solution (10 wt%) is prepared by dissolving 1 g PAN in 9 g DMF under magnetic stirring for 6 h. MnAc_2 is slowly added to PAN solution and keep stirring for 6 h. The mixed solution is held in a spinning nozzle with a tip diameter of 1 mm. A copper pin is connected to the anode of a high-voltage generator. A voltage of 20 kV is applied and the distance between the needle and collector is fixed value of 12 cm. A piece of aluminum foil is used as the collector. After the electrospinning process, a white color self-standing film of MnAc_2/PAN is obtained by flaking off the aluminum collector.

The stabilization of MnAc_2/PAN film is commonly performed in air at 250 °C for 1 h. The as-stabilized film is subsequently heated in N_2 atmosphere at various conditions described before. Under high temperature and inert atmosphere, PAN fiber is carbonized after the elements except carbon are removed. The Mn-oxide is produced together with the carbon fiber under high temperature. The final compositions of the product $\text{MnO}_x/\text{carbon}$ fiber are dependent on the precursors and the carbonized conditions that listed in Table 1.

By using Rigaku diffractometer with Cu K_α radiation, the X-ray diffraction data are collected at 0.02° step width from 10 to 80°. The morphology is characterized by using scanning electron microscope (SEM, Hitachi-X650 microscope, 20 kV). FT-IR spectra are recorded on a BRUKER VECTOR 22 spectrometer. The contents of carbon, hydrogen and nitrogen elements in the product are measured by elemental analyzer (Elementar VarioEL III, Germany).

Electrochemical performances of the samples are collected in CR2016 coin cells. The as-synthesized black film of $\text{MnO}_x/\text{carbon}$

Table 1
The elemental analysis results of the samples carbonized at various conditions.

Sample	Starting percent of MnAc_2 in precursor	Reaction condition	Elemental analysis			MnO_x wt%
			C wt%	H wt%	N wt%	
Mn60_3h	60 wt%	700 °C for 3 h	37.99	0.931	8.456	52.6
Mn50_3h	50 wt%	700 °C for 3 h	40.96	0	10.48	48.6
Mn40_3h	40 wt%	700 °C for 3 h	45.89	1.721	9.825	42.6
Mn33_3h	33 wt%	700 °C for 3 h	47.85	1.743	11.09	39.3
Mn33_1h	33 wt%	700 °C for 1 h	49.69	2.679	5.419	42.2
Mn33_6h	33.3 wt%	700 °C for 6 h	35.82	1.828	6.335	56.0
Mn33_12h	33.3 wt%	700 °C for 12 h	36.45	2.056	5.447	56.0

fiber after carbonization is directly used as electrode without any binder and conductive additive. Lithium foil is used as the counter electrode, 1 M LiPF₆ in EC: DMC = 1:1 as the electrolyte, and Celgard C480 membrane as the separator. Coin cells are assembled in an argon-filled glove box. Charge/discharge and cycle performances of the testing cells are carried out on Land CT2001A battery testing system. The cell is galvanostatically cycled between 0 and 3.0 V vs. Li/Li⁺ at current densities from 20 to 1000 mA g⁻¹.

3. Results and discussion

Polyacrylonitrile (PAN) fiber is the mostly used precursor for carbon fiber fabrication. Conversion of PAN molecules to carbon fibers requires a critical thermal stabilization stage which has great influence on the final morphology and properties of the carbon fibers [26,27]. In this work, after electrospinning manganese cations mixed with PAN molecules together produce a self-standing film. In the subsequent heat treatment, the cyclization, dehydration, oxidation and crosslinking in PAN are occurred almost simultaneously in the formation of manganese oxides enwrapped in the fibers.

Table 1 lists the elemental analysis results of the samples carbonized at various conditions. After carbonization, the white MnAc₂/PAN film shows much more weight loss and change to black color, involving to remove the non-carbon elements in nitrogen atmosphere. The composite fibers shrink in diameter (as shown in the following SEM section) and the weight loss is dependent on the precursor and carbonized conditions. As listed in Table 1, for the starting percent 33.3 wt% of MnAc₂ in precursor, the remained C wt % is 49.69, 47.85, 35.82, and 36.45% after carbonization for 1, 3, 6, and 12 h, respectively. It observes more manganese component remaining in the precursors with higher starting percent of MnAc₂ after carbonization at the same heat-treatment. For example, the sample with the starting MnAc₂ in precursors 60, 50, 40 and 33 wt% remains 47.85, 45.69, 40.96 and 37.99% in the final products of MnO_x/carbon, respectively.

Fig. 1 shows the XRD patterns of the as-synthesized MnO_x/carbon from the precursors with various weight ratios of MnAc₂ and PAN. Except the sample Mn30_3h with the lowest manganese content in precursor, all the XRD patterns of Mn60_3h, Mn50_3h and Mn40_3h are well indexed by the tetragonal-phase of Mn₃O₄ (JCPDS No. 24-0734) and the co-existing face-centered cubic phase of MnO (JCPDS No. 07-0230). Moreover, lower manganese content is in the precursor, more MnO phase appears in the product,

estimated from the relative intensity ratio of the characteristic peaks of MnO and Mn₃O₄ using MDI Jade software. In this work, it is hard to define the ratio between MnO and Mn₃O₄ based on the relative intensities of the characteristic XRD peaks which Barakat used in their work [28]. As shown in Fig. 1, the broad and low intensity diffraction peak in the range of 20–30° is associated with the presence of amorphous carbon, which is originated from the carbonization of PAN molecules. All the observed XRD patterns present broadened peaks with lower peak intensity and bigger FWHM (full width at half maximum). It indicates nanosized crystal MnO|Mn₃O₄ is grown in the presence of PAN fibers, especially, smaller crystal size MnO_x appeared in the precursor with lower manganese content. The different phases and the intensity ratio in XRD patterns suggest that the precursor compositions have a significant effect on the composite structure.

Based on the measured elemental analysis results, there is a large amount of MnO_x content in Mn33_3h synthesized from the lowest manganese content in precursor. None of any XRD peaks related with MnO_x are observed in Mn33_3h, except a broad peak near 24° observed which is attributed to amorphous carbon. It might be two possible reasons, nanosized MnO_x with smaller crystal size grown and enwrapped in carbon fiber during the simultaneously carbonization of PAN and growth of MnO_x nanocrystals; the other is amorphous MnO_x phase grown in carbon fiber because the carbonization time of 3 h is not enough for the crystal growth of MnO_x. For further discuss the question, we prolong the carbonization time to the precursor MnAc₂/PAN.

Fig. 2 presents the XRD profiles of the samples Mn33_1h, Mn33_3h, and Mn33_6h which carbonized at 700 °C for 1, 3, and 6 h, respectively. The three samples show the broad and low intensity diffraction peak in the range of 20–30° associated with the presence of amorphous carbon. After longer carbonization time of 6 h, the XRD patterns of manganese oxide are observed in Mn33_6h, which are well indexed to the face-centered cubic phase of MnO and the very weak XRD peaks are indexed to the tetragonal-phase of Mn₃O₄.

The manganese concentrations in precursor and carbonization times are both important factors to affect the phase and the size of MnO_x nanoparticles with carbon fibers. The exact formation mechanism of the MnO_x/carbon is complex and not fully understood. Based on the previous studies [29], the reactions involved in the process to form MnO|Mn₃O₄ are modified as follows:

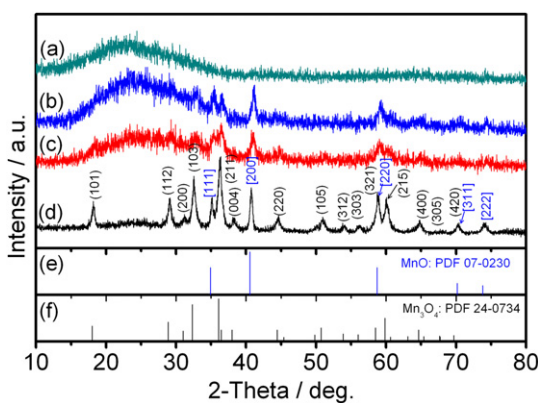


Fig. 1. XRD profiles of the samples (a) Mn33_3h, (b) Mn40_3h, (c) Mn50_3h, and (d) Mn60_3h synthesized at 700 °C for 3 h (e) and (f) the standard data of MnO and Mn₃O₄ from JCPDS card no. 07-0230 and 24-0734, respectively. The peaks in parenthesis are indexed by the tetragonal-phase of Mn₃O₄. The peaks in the square bracket are indexed to the co-existing face-centered cubic phase of MnO.

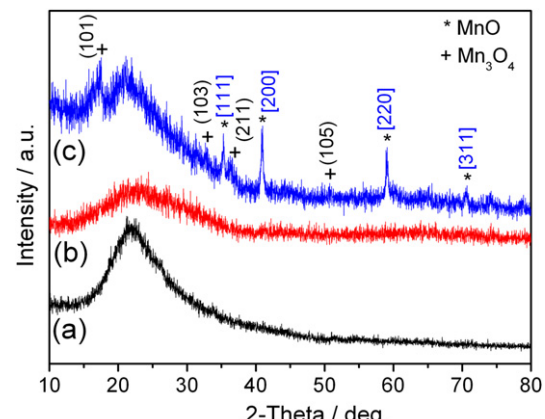
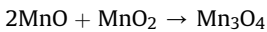
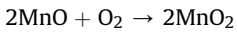


Fig. 2. XRD profiles of the samples (a) Mn33_1h, (b) Mn33_3h, and (c) Mn33_6h carbonized at 700 °C for 1, 3, and 6 h, respectively. The peaks in the square bracket are indexed to the face-centered cubic phase of MnO. The peaks in parenthesis are indexed by the co-existing tetragonal-phase of Mn₃O₄.



During the heat-treatment in air and the subsequent inert atmosphere, manganese acetate is mostly dehydrolyzed and decomposed to produce MnO, accompanied with the appearance of a large quantity of smoke above 200 °C. During the stabilization of MnAc₂/PAN film performed in air, only partial MnO₂ is generated from the reaction of MnO and O₂ because of the lower pre-heat treatment temperature of 250 °C and short time of 1 h. After the as-stabilized film is subsequently heated in N₂ atmosphere, MnO₂ is thoroughly reacted with MnO to produce Mn₃O₄.

In this work, the self-standing films of MnAc₂/PAN before and after carbonization are obtained. During the carbonization process at high temperature and inert atmosphere, the elements such as N and H of MnAc₂/PAN fibers are removed. Similar with the previous

work, the diameter of the fibers is decreased, but the chain-like carbon skeleton of PAN is still remained [10,27]. The SEM images of the samples MnO_x/carbon nanofiber are shown in Fig. 3. Along with the increased concentration of manganese in the precursors MnAc₂/PAN, the diameters of the carbonized MnO_x/carbon fiber are decreased. For the sample obtained from high manganese concentration in precursor, the carbon fibers are observed co-existence with manganese particles (as shown in Fig. 3c''). Along with the decreasing manganese concentration in precursor, the morphology of the product presents more nanofibers of MnO_x/carbon (as shown in Fig. 3d'–d''). The lower manganese concentration in MnAc₂/PAN is beneficial for the formation of MnO_x/carbon fiber through the procedures of electrospinning, heat-treatment and carbonization. The other difference in morphology of the sample synthesized from different ratios of MnAc₂ with PAN is the diameter of the fibers. By statistically estimating from the SEM images, the diameters are 130, 170, 250 and 350 nm in the

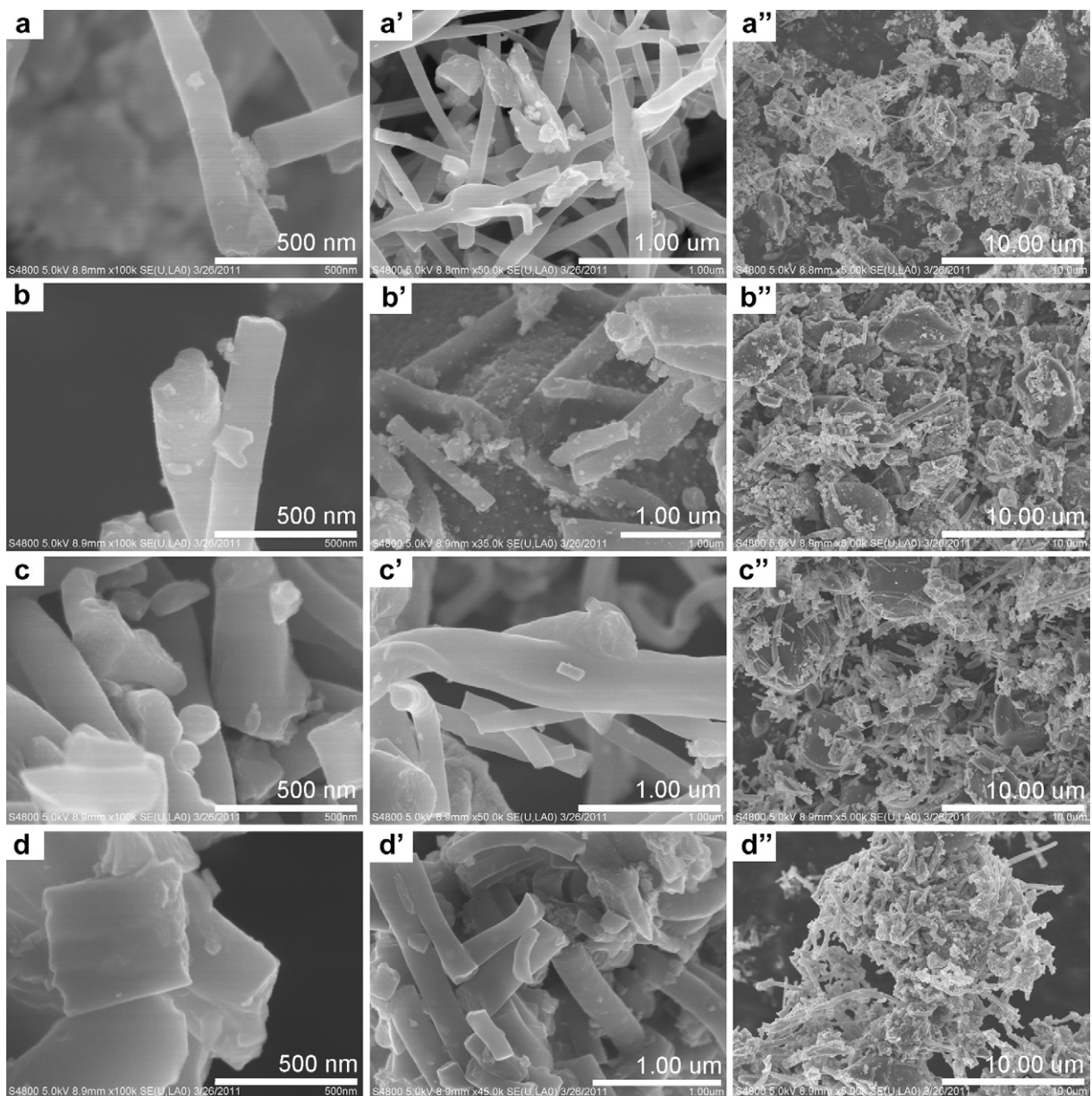


Fig. 3. SEM images of the samples of (a–a'') Mn60_3h, (b–b'') Mn50_3h, (c–c'') Mn40_3h, and (d–d'') Mn33_3h, respectively. The images with various magnifications show the detail information about carbon nanofibers and the composite of MnO_x/carbon.

samples Mn60_3h, Mn50_3h, Mn40_3h and Mn33_3h, respectively. The largest diameter of fiber in Mn33_3h is attributed from nanoparticles or amorphous MnO_x enwrapped in carbon fibers (as shown in Fig. 3d) which has been discussed by XRD patterns and elemental analysis results.

Fig. 4 shows the SEM images of the samples Mn33_1h, Mn33_3h, Mn33_6h and Mn33_12h carbonized at 700 °C for 1, 3, 6 and 12 h, respectively. Along with the prolonged carbonization time, the morphology of MnO_x /carbon fiber is well remained, and the surface of the fiber become more smooth (as shown in Fig. 4a'–d'). It can be noted that the diameters of MnO_x /carbon fibers are decreased along with the carbonization time. The calculated average diameters of the fibers in Mn33_1h, Mn33_3h, Mn33_6h and Mn33_12h are 400, 350, 250 and 200 nm, respectively. The decreased fiber diameters are attributed to the removed extent of N and H elements in PAN molecules which are obviously

dependent on the carbonization time. The diameters of MnO_x /carbon fibers shown in SEM well agree with the elemental analysis results discussed in the previous section. During carbonization, nanoparticles and/or amorphous MnO_x are well enwrapped in the carbon fibers, which the construction structure provides a “buffer zone” for the volume change of MnO_x during charge (delithiation) and discharge (lithiation) processes. But for a various carbonization time, the diameters of carbon fiber, that is the “buffer zone”, are changed. The relative electrochemical performance of MnO_x /carbon will be changed too, which is discussed in the following section.

The manufacture of MnO_x /carbon fibers from $MnAc_2$ /PAN precursors is mainly composed of two steps including thermal stabilization and carbonization. The first step (stabilization) involves heating the $MnAc_2$ /PAN fibers to 250 °C in air atmosphere to further orient, oxidation, and cyclization of PAN molecules,

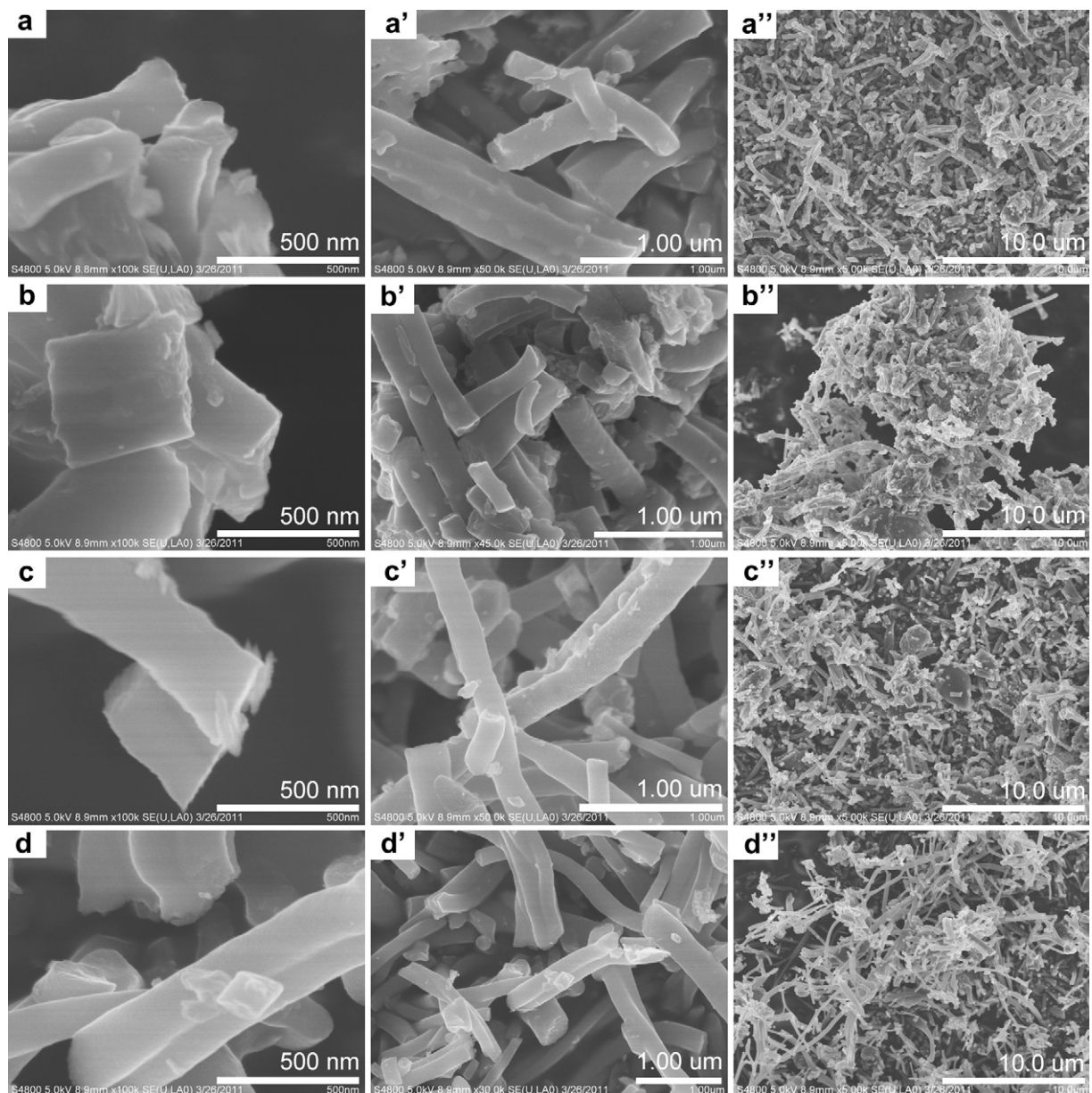


Fig. 4. SEM images of the samples (a–a'') Mn33_1h, (b–b'') Mn33_3h, (c–c'') Mn33_6h and (d–d'') Mn33_12h carbonized at 700 °C for 1, 3, 6 and 12 h, respectively. The images with various magnifications show the detail information about carbon nanofibers and the composite of MnO_x /carbon.

which can avoid the decomposing of PAN under the subsequent high-temperature pyrolysis. During the stabilization process, PAN molecules in the composite of MnAc₂/PAN film undergoes a number of physical and chemical changes that convert the linear PAN molecular chains to an aromatic ladder structure suitable for further carbonization and conversion to carbon fibers. Although the chemistry of stabilization process is complex including exothermic chemical reactions, cyclization, dehydration, oxidation and cross-linking among the polymer chains, FT-IR spectroscopy has proven to be an excellent technique to study the structural evolution of PAN fibers during the stabilization [26–28]. The main functional groups of MnO_x/PAN fibers are identified and characterized by the FT-IR technique. The FT-IR spectra of the sample MnAc₂/PAN before and after heat-treatment at 250 °C in air and 700 °C in nitrogen are shown in Fig. 5, which reflect the change of PAN molecules and decomposing of MnAc₂.

Fig. 5a is the FT-IR of self-standing film MnAc₂/PAN. The spectra show the main chemical group assignments for MnAc₂/PAN composite, which are identified and have the same polymeric structure with pure PAN fibers. The assignment at 2246 cm⁻¹ is attributed to the C≡N stretching of acrylonitrile unit in PAN chains. The bands at 1405 and 1337 cm⁻¹ are assigned to the vibrations of δ_{C–H} in CH₂ and ω_{C–H} in CH, respectively. The absorption at 1569 cm⁻¹ is attributed to stretching vibration of C–C. The weak band at 1740 cm⁻¹ is related to C=O or C–O bonds of the acetate of MnAc₂ [30,31]. The region below 1400 cm⁻¹ contains peaks due to fundamental vibrations of octahedral MnO₆ [32,33]. The bands range from 750 to 600 cm⁻¹ and 600 to 500 cm⁻¹ correspond to stretching and bending vibrations of Mn–O in MnAc₂. The samples with four different manganese concentrations in MnAc₂/PAN present similar FT-IR spectra, except some peak intensities. It can be observed the relatively stronger peaks related with PAN and weaker peaks related with MnAc₂ in Mn33_3h than those in Mn60_3h (as shown in Fig. 5a). For example, the peak intensities of ν_{C≡N} (at 2246 cm⁻¹) and ν_{Mn–O} (at 663 cm⁻¹) present opposite change in the film of MnAc₂/PAN with various manganese concentrations.

After heat-treatment at 250 °C for 1 h in air, the FT-IR spectra present much change accompany with removing of N and H elements during the stabilization, oxidation and cyclization of PAN molecules and the decomposing of MnAc₂. It is observed in Fig. 5b,

the band near 2242 cm⁻¹ related to stretching vibration of C≡N has an enormous decrease in intensity and shifts a little to higher wavelength near 2373 cm⁻¹. In the meantime, both bands at 1405 and 1337 cm⁻¹ assigned to δ_{C–H} in CH₂ and ω_{C–H} in CH (shown in Fig. 5a) become one band at 1382 cm⁻¹ assigned to δ_{C–H} in CH (shown in Fig. 5b) after the heat treatment at 250 °C in air, corresponding to stabilization and cyclization of PAN. Due to the cyclization of PAN molecules, the absorption related to the stretching vibration of C–C shifts to 1569 cm⁻¹ [27]. The band at 1740 cm⁻¹ related to C=O or C–O bonds is gone due to the decomposition of acetate, but a new weak band at 1145 cm⁻¹ is assigned to C–O bonds of oxidation of PAN molecules. The absorption of the Mn–O lattice vibrations around at 612 and 508 cm⁻¹ is indicative of a tetragonal distorted cubic lattice. These absorption peaks may be associated with the coupling mode between Mn–O stretching modes of tetrahedral and octahedral sites in Mn₃O₄ [34]. The main difference in the samples with various manganese concentrations is the relative intensity of peaks related with Mn–O bonds as shown in Fig. 5b.

In the subsequent carbonization at 700 °C, the elements of N, H and O are almost removed from the precursor. As shown in Fig. 5c, the band near 2380 cm⁻¹ related to the stretching vibration of C≡N is further weakened. The obviously weakened band at 1395 cm⁻¹ assigned to δ_{C–H} in CH (shown in Fig. 5c) still appears even after carbonization at 700 °C for 3 h, which minor H is well agree with the previous elemental analysis results. The new peak is observed at 1618 cm⁻¹ corresponding to the vibration of carbon backbone. After carbonization, the vibrations related to Mn–O bonds are obviously strengthened, and the peak positions are dependent on the manganese concentration in the products. For example, bands of 650 and 520 cm⁻¹ appear in Mn33_3h, 600 and 505 cm⁻¹ in Mn40_3h, 704 and 561 cm⁻¹ in Mn50_3h, and 610 and 500 cm⁻¹ in Mn60_3h, which are attributed to the different situation of Mn–O bonds of MnO and Mn₃O₄ in the final products of MnO_x/carbon fibers. Moreover, new band appears at 1165 cm⁻¹ after heat-treatment, it might be assigned to the bond of Mn–O–C in the composites. It further confirms that much smaller nanocrystals or amorphous MnO_x are grown and enwrapped in carbon fibers even which doesn't present any XRD peaks in Fig. 1a.

Fig. 6 shows the FT-IR spectra of the samples Mn33_1h, Mn33_3h, Mn33_6h after carbonized at 700 °C for 1, 3, and 6 h,

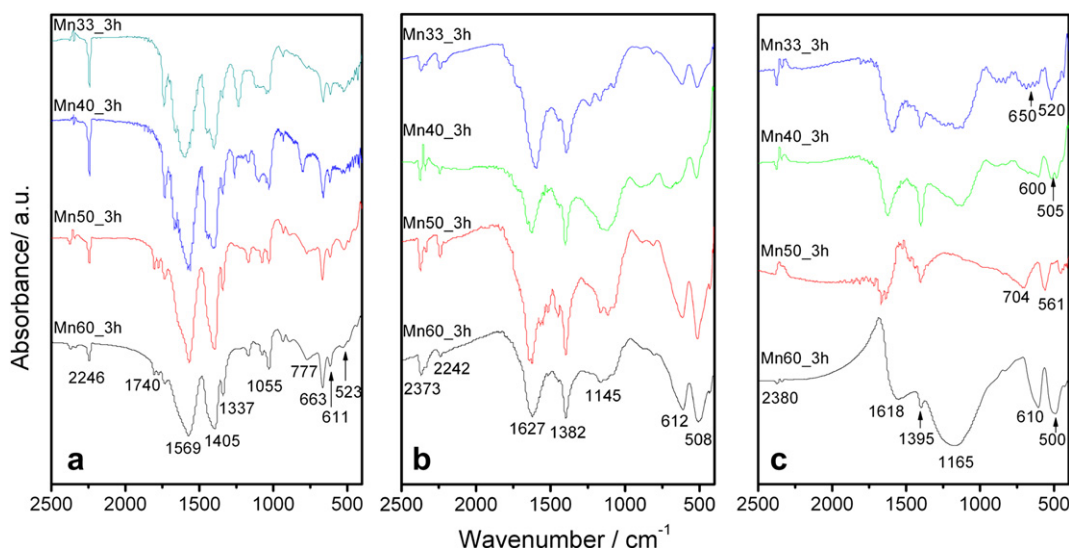


Fig. 5. FT-IR spectra of the samples MnAc₂/PAN before (a) and after heat-treatment at 250 °C in air (b), and 700 °C for 3 h in nitrogen atmosphere (c). The samples with four manganese concentrations in precursor are listed in the figures.

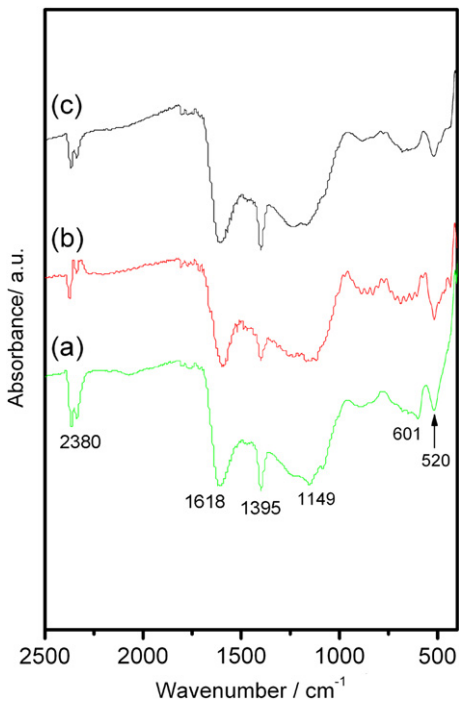


Fig. 6. FT-IR spectra of the samples (a) Mn33_1h, (b) Mn33_3h, and (c) Mn33_6h carbonized at 700 °C for 1, 3, and 6 h, respectively.

respectively. The three samples present similar FT-IR spectra. For example, the weak band at 2380 cm^{-1} is attributed to the stretching vibration of $\text{C}\equiv\text{N}$, 1618 cm^{-1} is the vibration of $\text{C}=\text{C}$ backbone of carbon fiber, and 1393 cm^{-1} is the remained vibration of $\text{C}-\text{H}$. For the prolonged carbonization time, the elements of N, H and O are removed more, corresponding to the weakened vibration of $\text{C}\equiv\text{N}$ and $\text{C}-\text{H}$ as shown in Fig. 6a and c. The three samples with

the same manganese concentration in their precursor, present the same peak position at 601 and 520 cm^{-1} related to $\text{Mn}-\text{O}$ bonds, corresponding to the same $\text{Mn}-\text{O}$ situation in the three samples. It indicates that the phase composition of MnO and Mn_3O_4 is mainly dependent on the manganese concentration in the precursors, instead of the carbonization conditions.

The above characterization of the $\text{MnO}_x/\text{carbon}$ samples describes the composition, crystal structure, morphology of the fibers are much dependent on the concentration of manganese in the precursors. The following electrochemical performances present the similar dependence. Fig. 7 shows the 1st, 5th, 20th and 50th charge and discharge profiles and cycle performance of $\text{MnO}_x/\text{carbon}$ with various manganese contents at a constant current density of 50 mA g^{-1} . At the first discharge (lithiation), all the samples deliver higher discharge capacities, 1054.1, 1019.0, 967.8, and 1113.3 mAh g^{-1} in Mn33_3h, Mn40_3h, Mn50_3h and Mn60_3h, respectively. Three voltage ranges, such as 3–0.8, 0.8–0.3 and 0.3–0 V vs. Li^+/Li are observed in the initial discharge curves of Fig. 7, which the first is attributed to the formation of solid electrolyte interphase (SEI) film and other inactive materials [10,22,35,36], and the last two curves are the insertion of lithium with $\text{MnO}_x/\text{carbon}$ composite [23]. For example, the initial discharge and charge capacities of the sample Mn33_3h are 1054.1 and 665.6 mAh g^{-1} , respectively. The low coulombic efficiencies (63%) of $\text{MnO}_x/\text{carbon}$ in the first cycle are usually attributed to the formation of a solid electrolyte interphase (SEI) layer and the pulverization of the active materials [13,37].

The sample of Mn33_3h with the lowest manganese content delivers the best electrochemical properties. For example, the initial charge capacities are 665.6, 624.8, 503.1, and 527.4 mAh g^{-1} in Mn33_3h, Mn40_3h, Mn50_3h and Mn60_3h, respectively. After the initial cycle, the sample Mn33_3h presents almost overlapped charge and discharge curves as shown the 5th, 20th and 50th cycles in Fig. 7, which indicates the well reversibility during Li insertion and extraction. The sample Mn60_3h with highest manganese contents presents poor initial coulombic efficiency (47%) and lower

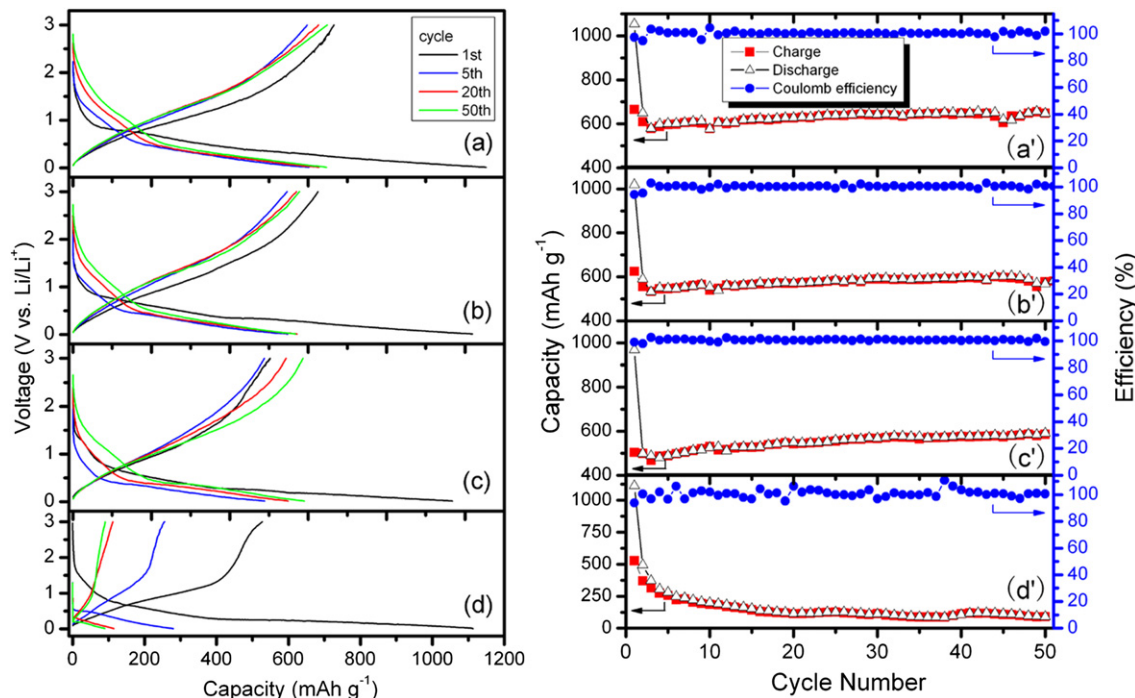


Fig. 7. The specific charge/discharge profiles, cycle performance and coulombic efficiency of the samples, (a) and (a') Mn33_3h, (b) and (b') Mn40_3h, (c) and (c') Mn50_3h, and (d) and (d') Mn60_3h, carried out at a constant current density of 50 mA g^{-1} .

reversible capacity, though it shows the highest initial discharge capacity of $1113.3 \text{ mAh g}^{-1}$.

As shown in Fig. 7a'–d', Mn33_3h, Mn40_3h and Mn50_3h present a well cycle performance without capacity loss after 50 cycles, except the sample Mn60_3h. After the initial cycle, the coulombic efficiency of the following cycles is near 100% (as shown in Fig. 7a'–d'). The sample Mn33_3h presents the best cycleability which retains a discharge capacity of 646.6 mAh g^{-1} after 50 cycles (99.7% of the 2nd discharge capacity 648.7 mAh g^{-1}), compared with 582.2 mAh g^{-1} in Mn40_3h, 590.7 mAh g^{-1} in Mn50_3h, and 89.8 mAh g^{-1} in Mn60_3h at the 50th cycle. It further indicates that the morphology of MnO_x /carbon fiber is an important factor for the electrochemical performance. There is a well composite structure in the sample Mn33_3h where nanoparticles and/or amorphous MnO_x are enwrapped in the carbon fibers. The construction structure well improves the conductivity of MnO_x particles and provides a “buffer zone” for the volume change of MnO_x during lithiation and delithiation. As statistically estimated diameters of MnO_x /carbon fibers are 130, 170, 250 and 350 nm in the samples Mn60_3h, Mn50_3h, Mn40_3h and Mn33_3h, the 50th charge capacities are 648.9 , 580.8 , 586.4 , and 90.6 mAh g^{-1} , respectively.

The carbonization is another important factor to the electrochemical performance for the samples MnO_x /carbon. Fig. 8 shows the specific charge/discharge profiles and cycle performance of Mn33_1h, Mn33_3h, Mn33_6h and Mn33_12h carbonized at 700°C for 1, 3, 6 and 12 h, respectively. The proper carbonization time will produce the good morphology of MnO_x nanoparticles co-existence with carbon fibers. Longer carbonization time results in the bigger MnO_x crystals and smaller fiber diameter, because more elements of N and H are removed which has been shown in XRD patterns and SEM images. The electrochemical performance shows the relative change. For example, the initial charge capacities of Mn33_1h, Mn33_3h, Mn33_6h and Mn33_12h are 879.6 , 1054.1 , 978.2 , and $1001.7 \text{ mAh g}^{-1}$, respectively. Moreover, well cycle performance is observed in the sample Mn33_3h. For example, the 50th charge capacities of Mn33_1h, Mn33_3h, Mn33_6h and

Mn33_12h are 529.4 , 648.9 , 581.7 and 550.9 mAh g^{-1} , compared with the initial charge capacities of 600.0 , 665.6 , 618.8 , and 603.3 mAh g^{-1} , respectively. The samples of Mn33_3h and Mn33_6h present better capacity and cycleability than Mn33_1h and Mn33_12h. Mn33_1h contains more elements of N and H for the shorter carbonization time. The composite structure of Mn33_12h with smaller diameter of carbon fiber and bigger crystal size of MnO_x is not beneficial for lithiation and delithiation of MnO_x /carbon due to the smaller “buffer zone”.

Fig. 9 shows the initial charge/discharge profiles and cycle performance of the sample Mn33_3h carbonized at the temperature of 500 , 600 , 700 and 800°C , respectively. The samples are carried out at a constant current density of 50 mA g^{-1} . The sample Mn33_3h synthesized at 700°C presents the best electrochemical performance. For example, the initial charge capacities are 91.6 , 342.1 , 665.6 , and 597.0 mAh g^{-1} in the samples carbonized at 500 , 600 , 700 and 800°C , respectively. We believe a proper carbonization temperature is beneficial for the formation of MnO_x nanoparticles enwrapped in carbon fibers. Proper temperature can improve the carbonization extent of PAN and the formation of MnO_x . The samples produced at 700 and 800°C still deliver 646.6 and 600.7 mAh g^{-1} at the 50th cycle, which is much higher than 110.7 and 402.3 mAh g^{-1} of the samples carbonized at 500 and 600°C , respectively.

The rate capability, which is always important for practical applications, is evaluated. Fig. 10 shows the representative discharge/charge profiles, cycle performance and coulombic efficiency of Mn33_3h at current densities of 20 , 100 , 400 and 1000 mA g^{-1} , respectively. When the current densities are increased from 20 , 100 , 400 , and 1000 mA g^{-1} , the corresponding charge capacities are 687.4 , 450.4 , 256.5 , and 116.4 mAh g^{-1} , respectively. In all of the cycles at various current densities, the coulombic efficiency is close to 100%. The other important result is the recovery of the sample Mn33_3h after high rate cycling at 1 A g^{-1} . When the current density is back to 20 mA g^{-1} after 5 charge/discharge cycles at 1 A g^{-1} , the cell recovers full charge

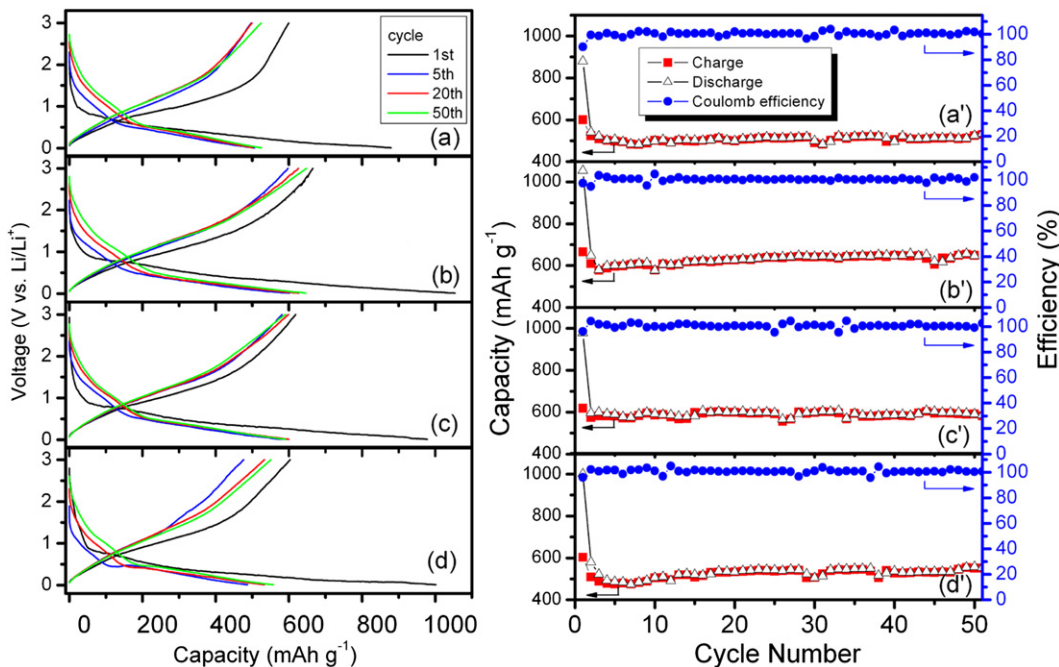


Fig. 8. The specific charge/discharge profiles, cycle performance and coulombic efficiency of the samples, (a–a'') Mn33_1h, (b–b'') Mn33_3h, (c–c'') Mn33_6h, and (d–d'') Mn33_12h carbonized at 700°C for 1, 3, 6, and 12 h, respectively. The samples are carried out at a constant current density of 50 mA g^{-1} .

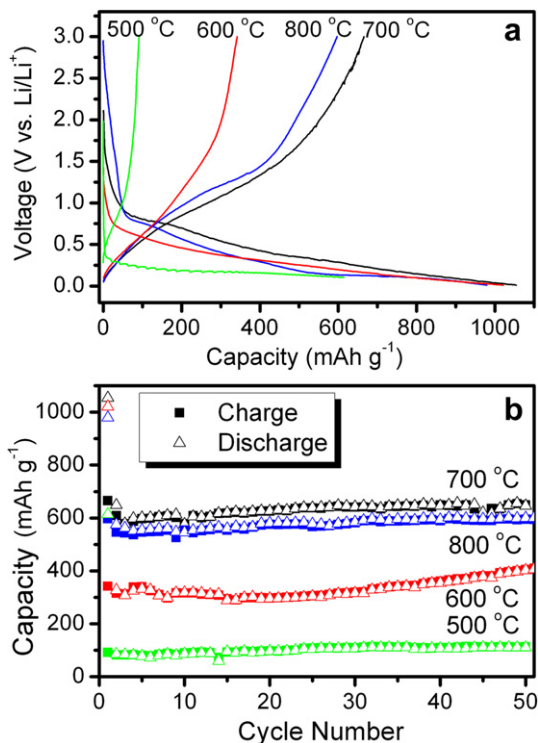


Fig. 9. The initial charge/discharge profiles (a) and cycle performance (b) of the sample Mn33_3h carbonization at the temperature 500, 600, 700 and 800 °C, respectively. The samples are carried out at a constant current density of 50 mA g⁻¹.

capacity of 661.7 mAh g⁻¹ at 20 mA g⁻¹, indicating the stability of the anode in a wide range of current densities. The outstanding electrochemical performance is attributed to the composite structure of MnO_x nanoparticles enwrapped in carbon fibers, which provide a void space for the volume change of MnO_x during

lithiation and delithiation. The advantages of this composite structure as well as its high capacity make manganese oxide a very attractive candidate as an anode material for the next generation of rechargeable lithium ion batteries, and can be widely used in the preparation of other transition metal oxide/carbon materials.

4. Conclusions

Through electrospinning, the precursors of MnAc₂/PAN with various manganese contents are synthesized. After thermal stabilization (at 250 °C in air) and carbonization (at 700 °C in nitrogen), one-dimensional composites MnO_x/carbon are converted from MnAc₂/PAN precursors. The phase composition, morphology, growth mechanism and electrochemical performance of the product MnO_x/carbon are greatly affected by the manganese concentration in precursor and the subsequent carbonization conditions. The main functional groups such as CN, CH, and Mn–O of the sample in three stages of precursor MnAc₂/PAN, stabilization and carbonization, present the detailed information in their FT-IR spectra. The change of intensity and peak position of Mn–O in the three stages indicate the bond situation and growth of manganese oxides. The sample of Mn33_3h with the lowest manganese content presents the excellent electrochemical properties. The initial charge and discharge capacity of Mn33_3h are 1054.1 and 665.6 mAh g⁻¹, and the discharge capacity at the 50th cycle remains 99.7% of that at the 2nd cycle. However, Mn40_3h, Mn50_3h and Mn60_3h present relatively lower capacities and poor cycleability. The composite structure well improves the conductivity of MnO_x particles and provides a “buffer zone” for the volume change of MnO_x during lithiation and delithiation, which is an efficient way to improve the cell capacity and cycleability. Beside the well rate capability at the range of current densities from 20 to 1000 mA g⁻¹, Mn33_3h presents very good recovery ability after high rate cycling at 1000 mA g⁻¹. The advantages of this composite structure as well as its high capacity make manganese oxide a very attractive candidate as an anode material for the next generation of rechargeable lithium ion batteries, and can be widely used in the preparation of other transition metal oxide/carbon materials.

Acknowledgments

We acknowledged the grant provided by Fundação para a Ciéncia e Tecnologia (Portugal) (SFRH/BPD/64217/2009). The work was supported by NSF of Jiangsu Province of China (Grant No. BK2010262), NSF of Jiangsu Educational Department of China (Grant No. 10KJA480001), and NSF of China (Grant No. 51172032).

References

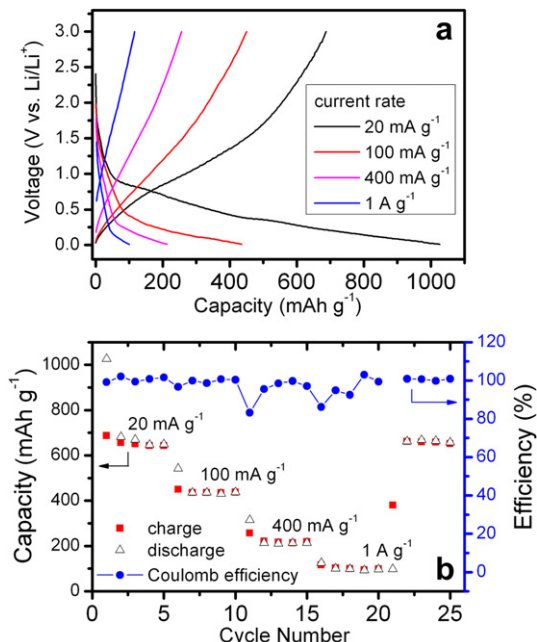


Fig. 10. The initial charge/discharge profiles (a), cycle performance and coulombic efficiency (b) of the sample Mn33_3h carried out at constant current densities of 20, 100, 400 and 1000 mA g⁻¹, respectively.

- [1] K.E. Aifantis, S.A. Hackney, R.V. Kumar (Eds.), *High Energy Density Lithium Batteries: Materials, Engineering, and Applications*, Wiley-VCH, 2010.
- [2] R. Fong, R.U. von Sacken, J.R. Dahn, *J. Electrochem. Soc.* 137 (1990) 2009.
- [3] W.J. Zhang, *J. Power Sources* 196 (2011) 13.
- [4] P. Poizot, S. Laruelle, S. Gruegeon, L. Dupont, J.-M. Tarascon, *Nature* 407 (2000) 496.
- [5] K.T. Nam, D.P. Kim, J. Yoo, C. Chiang, N. Meethong, P.T. Hammond, Y. Chiang, A.M. Belcher, *Science* 312 (2006) 885.
- [6] P. Meduri, C. Pendyala, V. Kumar, G.U. Sumanasekera, M.K. Sunkara, *Nano Lett.* 9 (2009) 612.
- [7] C. Ban, Z. Wu, D.T. Gillaspie, L. Chen, Y. Yan, J.L. Blackburn, A.C. Dillon, *Adv. Mater.* 22 (2010) E145.
- [8] J. Zhong, C. Cao, Y. Liu, Y. Li, W.S. Khan, *Chem. Commun.* 46 (2010) 3869.
- [9] S. Wang, J. Zhang, C. Chen, *J. Power Sources* 195 (2010) 5379.
- [10] H.Y. Wang, P. Gao, S.F. Lu, H.D. Liu, G. Yang, J. Pinto, X.F. Jiang, *Electrochim. Acta* 58 (2011) 44.
- [11] H. Li, P. Balaya, J. Maier, *J. Electrochem. Soc.* 151 (2004) A1878.
- [12] Q. Fan, M.S. Whittingham, *Electrochim. Solid State Lett.* 10 (2007) A48.
- [13] K.F. Zhong, X. Xia, B. Zhang, H. Li, Z.X. Wang, L.Q. Chen, *J. Power Sources* 195 (2010) 3300.

- [14] H.L. Wang, L.F. Cui, Y. Yang, H.S. Casalongue, J.T. Robinson, Y.Y. Liang, Y. Cui, H.J. Dai, *J. Am. Chem. Soc.* 132 (2010) 13979.
- [15] X.Q. Yu, Y. He, J.P. Sun, K. Tang, H. Li, L.Q. Chen, X.J. Huang, *Electrochem. Commun.* 11 (2009) 791.
- [16] P. Poizot, S. Laruelle, S. Grangeon, L. Dupont, J.M. Tarascon, *J. Electrochem. Soc.* 149 (2002) A1212.
- [17] D. Pasero, N. Reeves, A.R. West, *J. Power Sources* 141 (2005) 156.
- [18] Q. Fan, M.S. Whittingham, *Mater. Res. Soc. Symp. Proc.* (2007) 972.
- [19] J. Fan, T. Wang, C. Yu, B. Tu, Z. Jiang, D. Zhao, *Adv. Mater.* 16 (2004) 1432.
- [20] F. Cheng, Z. Tao, J. Liang, J. Chen, *Chem. Mater.* 20 (2008) 667.
- [21] H. Kawaoka, M. Hibino, H.S. Zhou, I. Honma, *J. Electrochem. Soc.* 152 (2005) A1217.
- [22] J. Gao, M.A. Lowe, H.D. Abruna, *Chem. Mater.* 23 (2011) 3223.
- [23] Z. Lin, L. Ji, M.D. Woodrooff, X.W. Zhang, *J. Power Sources* 195 (2010) 5025.
- [24] Y. Yu, L. Gu, C. Wang, A. Dhanabalan, P.A. Aken, J. Maier, *Angew. Chem. Int. Ed.* 48 (2009) 6485.
- [25] X.H. Zong, K. Kim, D.F. Fang, S.F. Ran, B.S. Hsiao, B. Chu, *Polymer* 43 (2002) 4403.
- [26] A. Sedghi, R.E. Farsani, A. Shokuhfar, *J. Mater. Process. Tech.* 98 (2008) 60.
- [27] M.S.A. Rahaman, A.F. Ismail, A. Mustafa, *Polym. Degrad. Stabil.* 92 (2007) 1421.
- [28] N.A.M. Barakat, K.D. Woo, S.G. Ansari, J.A. Ko, M.A. Kanjwal, H.Y. Kim, *Appl. Phys. A* 95 (2009) 769.
- [29] G.M. An, P. Yu, M.J. Xiao, Z.M. Liu, Z.J. Miao, K.L. Ding, L.Q. Mao, *Nanotechnology* 19 (2008) 275709.
- [30] S. Dalton, F. Heatley, P.M. Budd, *Polymer* 40 (1999) 5531.
- [31] M. Ji, C. Wang, Y. Bai, M. Yu, Y. Wang, *Polym. Bull.* 59 (2007) 527.
- [32] M. Minakshi, P. Singh, T.B. Issa, S. Thurgate, R.D. Marco, *J. Power Sources* 138 (2004) 319.
- [33] D.P. Dubala, D.S. Dhawale, R.R. Salunkhe, S.M. Pawar, V.J. Fulari, C.D. Lokhande, *J. Alloy. Compd.* 484 (2009) 218.
- [34] C.M. Julien, M. Massot, C. Poinsignon, *Spectrochim. Acta* 60 (2004) 689.
- [35] Y.S. Hu, R. Demir-Cakan, M.M. Titirici, J.O. Muller, R. Schlogl, M. Antonietti, J. Maier, *Angew. Chem. Int. Ed.* 47 (2008) 1645.
- [36] Q. Wang, L.J. Liu, L.Q. Chen, X.J. Huang, *J. Electrochem. Soc.* 151 (2004) A1333.
- [37] Y.H. Yu, Q. Yang, D.H. Teng, X.P. Yang, S. Ryu, *Electrochem. Commun.* 12 (2010) 1187.